Einstein–de Haas effect at radio frequencies in and near magnetic equilibrium

K. Mori [1], M. G. Dunsmore [1], J. E. Losby [1,2] D. M. Jenson,[1] M. Belov [2], and M. R. Freeman [1,*]
[1]*Department of Physics, University of Alberta, Edmonton, Alberta T6G 2E1, Canada*
[2]*Nanotechnology Research Centre, National Research Council of Canada, Edmonton, Alberta T6G 2M9, Canada*

The Einstein-de Haas (EdH) effect and its reciprocal, the Barnett effect, are fundamental to magnetism and uniquely yield measures of the ratio of magnetic moment to total angular momentum. These effects, small and generally difficult to observe, are enjoying a resurgence of interest as contemporary techniques enable new approaches to their study. The high mechanical resonance frequencies in nanomechanical systems offer a tremendous advantage for the observation of EdH torques in particular. At radio frequencies, the EdH effect can become comparable to or even exceed in magnitude conventional cross-product magnetic torques. In addition, the rf-EdH torque is expected to be phase shifted by 90 degrees relative to cross-product torques, provided the magnetic system remains in quasistatic equilibrium, enabling separation in quadratures when both sources of torque are operative. Radio-frequency EdH measurements are demonstrated through the full hysteresis range of micrometer-scale, monocrystalline yttrium iron garnet disks. Equilibrium behavior is observed in the vortex state at low bias field. Barkhausen-like features emerge in the in-plane EdH torque at higher fields in the vortex state, revealing magnetic disorder too weak to be visible through the in-plane cross-product torque. Beyond vortex annihilation, peaks arise in the EdH torque versus bias field, and these together with their phase signatures indicate additional utility of the Einstein-de Haas effect for the study of rf-driven spin dynamics.

I. INTRODUCTION

Einstein-de Haas (EdH) measurements on magnetic systems, historically, have been challenging [1–5], owing to the small magnitudes of EdH torques in relation to conventional cross products of field and moment vector magnetic torques. EdH measurements involve application of an alternating magnetic field *parallel* to a mechanical torsion axis to probe the intrinsic, microscopic coupling of magnetic moment and mechanical angular momentum in the sample. The angular momentum variation accompanying field-driven changes in the net moment is governed by the material's magnetomechanical ratio, $g\prime$ [6]. Determinations of $g\prime$ have been the primary motivation for EdH studies. There is also an opportunity to exploit the EdH effect to measure AC susceptibilities along the direction of an applied AC magnetic field.

A conventional magnetic torque experiment [7], by contrast, intrinsically measures magnetic anisotropies by sensing the magnetic potential energy variation versus angle for a magnetic object in an external applied field. Anisotropies can arise from specimen shape, composition, and microstructure via dipolar, spin-orbit, exchange, and interfacial couplings. When the anisotropy is known, the cross-product torque is useful for the determination of magnetic moment (torque magnetometry).

The ratio of net magnetic moment, m, to net angular momentum, J, in a magnetic material is given in terms of $g\prime$ by

$$\frac{m}{J} = g\prime \frac{e}{2m_{\mathrm{e}}} \equiv \gamma\prime, \tag{1}$$

where e and m_{e} are the electron charge and mass. We define this quantity as the spin-mechanical gyromagnetic ratio of the material, $\gamma\prime$, to position mechanical torque experiments on a parallel footing with spin-precession measurements. Simultaneous EdH and cross-product torque measurements as reported below represent an opportunity to determine $\gamma\prime$ directly via ratios of the mechanical signal amplitudes. The amplitudes are but half of the information contained in the signals, however, and phase-sensitive measurements are shown to be invaluable for distinguishing between the two different physical origins of torque.

The miniaturization of torque sensors that began late in the 20th century with silicon micromachining [8] has created new opportunities for study of the EdH effect. An elegant determination of $g\prime$ for a permalloy thin film was reported in 2006 by Wallis *et al.* [9], who deposited the sample on a silicon microcantilever and measured at the 13 kHz fundamental flexural resonance of that device. The EdH effect in a 23-kHz yttrium iron garnet (YIG) cantilever has been used to detect angular momentum pumping driven by the spin Seebeck effect [10]. Finally, the physics of the Barnett effect has been elucidated recently through inductively detected electron and nuclear spin resonance experiments, with and without the detection coil in the reference frame of the rotating specimen [11,12].

The present paper draws attention to distinguishing features of EdH torques that emerge as EdH experiments are miniaturized further, both in the quasistatic regime where the magnetic system remains at or near instantaneous equilibrium with the total applied field and as spin dynamics begin to emerge.

*mark.freeman@ualberta.ca
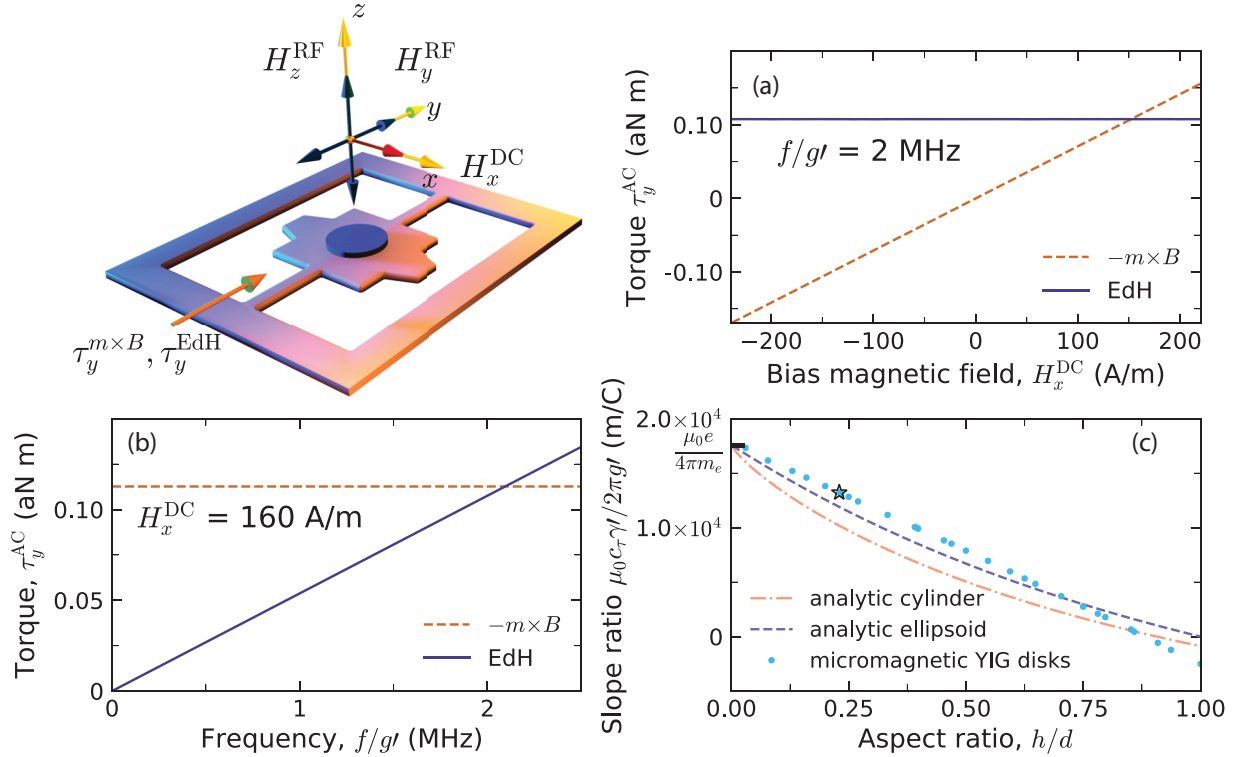
FIG. 1. Conceptual overview of simultaneous cross-product and EdH torque measurements on a micromagnetic disk supported by a mechanical torsion resonator. The rf and DC magnetic field geometry is illustrated at the upper left. H_y^{rf} drives the EdH torque, τ_y^{EdH}, while H_z^{rf} drives the cross-product torque, $\tau_y^{m \times B}$. The DC field along x is variable and swept for hysteresis measurements. (a) Simulated torques for a 2.1-μm-diameter by 490-nm-thick YIG disk with a magnetic vortex spin texture at low bias fields, showing the cross-product torque linear proportionality to field, and the EdH torque field strength independence. (b) Simulated torques as a function of frequency, showing the EdH torque strength proportionality to frequency, and the cross-product torque frequency independence. (c) The ratio of the linear slopes as in panels (b) and (c), as a function of sample geometry. The physical constant governing the overall scale of torque slope ratios is the inverse electron gyromagnetic ratio. Lines: Analytical results for cylinders and ellipsoids of revolution, assuming uniform magnetization. Symbols: A collection of micromagnetic simulations of YIG disks, including cubic anisotropy with an easy axis oriented along $\hat{z}$. The star corresponds to the aspect ratio used for panels (a) and (b). All torque amplitudes in this figure are calculated for rf drive field strengths of 80 A/m RMS.

II. SIMULTANEOUS EINSTEIN-DE HAAS AND CROSS-PRODUCT AC MAGNETIC TORQUES: CONCEPTUAL FRAMEWORK

A quantitative sense of the magnitude of the quasistatic rf-EdH effect for standard specimens is obtained by considering mechanical torque measurements on a disk of soft ferromagnetic material, in the configuration illustrated in the upper left panel of Fig. 1. The sample material is assumed to be magnetically isotropic with a constant volume susceptibility, χ, at low fields. The shape has magnetometric demagnetizing factors N_z and $N_r = (1 - N_z)/2$ in the axial and radial directions [13,14]. Application of rf and DC magnetic fields, $H_z^{\mathrm{rf}} \sin(\omega t)$ and H_x^{DC} to the disk, both assumed small enough to remain in the constant susceptibility regime, and taking $B = \mu_0 H$ for all external applied fields, yields the rf cross-product torque:

$$\tau_y^{m \times B} = -\left[\chi V (1 - N_r) H_x^{\mathrm{DC}}\right]\left[\mu_0 H_z^{\mathrm{rf}} \sin(\omega t)\right]$$
$$+ \left[\chi V (1 - N_z) H_z^{\mathrm{rf}} \sin(\omega t)\right]\left(\mu_0 H_x^{\mathrm{DC}}\right)$$
$$= -\mu_0 (N_z - N_r)\chi V H_x^{\mathrm{DC}} H_z^{\mathrm{rf}} \sin(\omega t). \qquad (2)$$

Equation (2) represents the resultant y torque after the contribution from the moment along x multiplied by the rf field along z (first term) is reduced by the induced rf moment along z multiplied by the DC field along x (the second term is significant outside the very thin film limit where $N_z \approx 1$). This same rf drive will generate an EdH mechanical torque along z (not measurable with the devices used here), according to

$$\tau_z^{\mathrm{EdH}} = -\frac{dJ_z}{dt} = -\frac{2m_e}{eg\prime}(1 - N_z)\chi V \omega H_z^{\mathrm{rf}} \cos(\omega t), \qquad (3)$$

where the minus sign comes from total angular momentum conservation of the combined magnetic/mechanical system in the absence of external torques.

The EdH torque of Eq. (3) reflects the rf magnetic susceptibility along $\hat{z}$. A linear increase with frequency of the relative amplitudes of EdH and cross-product torques is expected, along with a quadrature phase relationship between the two signals. Both consequences arise from the single time derivative of the mechanical angular momentum underlying the EdH torque.

The current experiment has a single torque-sensing axis and therefore a separate rf drive field, $H_y^{\text{rf}}\sin(\omega t)$, is used to excite an in-plane EdH torque,

$$\tau_y^{\text{EdH}} = -\frac{dJ_y}{dt} = -\frac{2m_e}{eg\prime}(1-N_r)\chi V \omega H_y^{\text{rf}}\cos(\omega t), \qquad (4)$$

We turn to numerical simulation of the torques with MU-MAX3 [15] to account for the influence of nonuniform spin textures, magnetocrystalline anisotropy, and other modifications beyond the simplest scenario. Results from a micromagnetic simulation of rf cross-product and EdH torques for a YIG disk of height-to-diameter aspect ratio 0.23 and in the vortex state are plotted in Figs. 1(a) and 1(b), respectively, versus low bias fields, H_x (omitting the superscript DC from this point forward), for fixed frequency and versus frequency, f, for fixed low bias field. These graphs emphasize the takeaway from Eqs. (2) and (3) that the torques are linearly proportional, respectively, to H_x and $f = \omega/2\pi$, and independent of the other parameter when the system remains quasistatically in magnetic equilibrium. The simulation predicts crossover of the EdH and cross-product torque magnitudes at $f/g\prime = 2$ MHz and $H_x = 160$ A/m, as a specific example.

An estimation of the relative torques for arbitrary shapes can be obtained from a plot of the ratio of these two slopes, which in the linear regime can be written

$$\frac{d\tau_y^{m\times B}/dH_x}{d\tau_y^{\text{EdH}}/df} = c_\tau \frac{\mu_0 \gamma\prime}{2\pi}, \qquad (5)$$

where c_τ is a sample-specific dimensionless constant accounting for anisotropy. In the analytic case presented above, $c_\tau = (N_z - N_r)/(1-N_r) = (1-3N_r)/(1-N_r)$.

When the two rf drives are of the same strength, the predicted ratio of the two torque amplitudes is

$$\frac{\tau_y^{m\times B}}{\tau_y^{\text{EdH}}} = c_\tau \frac{\gamma\prime \mu_0}{2\pi}\frac{H_x}{f}. \qquad (6)$$

An analog of the expression for Larmor precession arises for conditions where the torque magnitudes are equal and the left-hand side therefore equals unity. In the Larmor case, the frequency is governed by a ratio of magnetic torque to spin angular momentum, governed by the relevant spectroscopic splitting g factor and generally also with at least a small modification by a magnetic anisotropy term [16].

Figure 1(c) summarizes these results, and presents a quantity that is independent of the material-specific $g\prime$ by showing $(c_\tau \mu_0 \gamma\prime/2\pi g\prime)$ versus the height-over-diameter aspect ratio, h/d. (The division by $g\prime$ cancels the $g\prime$ built in to $\gamma\prime$.) The scale of torque slope ratios is anchored by $4\pi m_e/(\mu_0 e) = 17588$ m/C, for fields and frequencies measured in A/m and Hz. To describe any particular sample, the 17 588 m/C value is multiplied by the corresponding c_τ accounting for the aggregate anisotropy. The torque slope ratio decreases as the sample becomes more isotropic, for example, as a thin disk becomes taller and the cross-product torque decreases. In the case of the disk, this decrease of cross-product torque is slightly offset by a decrease of the in-plane susceptibility and hence of the EdH torque, as the disk becomes taller. As numerical examples in the limit of a thin disk with $h/d \sim 0$, and with $f/g\prime = 2$ MHz, the cross-product

torque will equal the EdH torque when $H_x \equiv H_{\text{crossover}} = 4 \times 10^6 \text{ s}^{-1}/(2 \times 17588 \text{ m/C}) = 114$ A/m. This is a very achievable condition for routine micromechanical magnetometry. In comparison, note that for the mechanical frequency of Ref. [9] (13 kHz), we would have $H_{\text{crossover}} = 0.37$ A/m (approximately 1/100 of Earth's field), and for that of the original EdH experiment (50 Hz), it would be about 1/25 000 of Earth's field.

Results from a series of micromagnetic simulations for YIG cylinders of various aspect ratios, all in the magnetic vortex spin texture, are shown by the closed symbols in Fig. 1(c). The cubic anisotropy is oriented to have an easy axis along z, which is also the axis of the vortex core. The open star demarcates the aspect ratio corresponding to the simulation results shown in Figs. 1(a) and 1(b). Again, to yield the same (y) component of torque, the AC drive field directions for EdH, cross-product torques in the calculation are along $\hat{y}$, $\hat{z}$, respectively. Analytical curves representing the expected ratio of cross-product and EdH AC torque magnitudes are presented also, for cylinders and ellipsoids of revolution of any soft ferromagnetic material having an isotropic volume susceptibility. The dashed curve for the ellipsoid of revolution has its zero crossing at aspect ratio = 1 (sphere), where the cross-product torque vanishes. The corresponding aspect ratio where the radial and axial demagnetizing factors for the cylinder are equal (where its axial and radial demagnetizing factors are equal) is $h/d = 0.9$. At low aspect ratio, the more rapid initial decrease of the torque slope ratio for ellipsoids versus cylinders reflects the more rapid increase of the radial demagnetizing factor for the cylinders as the height increases.

Qualitatively, the torque slope ratio from the simulations at low aspect ratio is closer to the analytical result for the ellipsoids of revolution; the vortex texture helps sustain the ease of magnetizing in plane, initially as the height increases. The taller YIG disks show a net-zero cross-product torque at an aspect ratio close to that of the analytical cylinders. The vortex texture and cubic anisotropy conspire overall to yield a more linear decrease of the torque slope ratio versus aspect ratio, in comparison to either of the analytical results. The contributions of the spin texture and anisotropy are not fully independent, in modifying the torques over the simple analytical case. For the sample orientation in this study, having a magnetocrystalline easy axis parallel to the cylinder axis, negative K_c also helps to stabilize the vortex texture in taller cylinders. The coupling of these effects underscores the importance of performing micromagnetic simulations of the torques.

III. EXPERIMENTAL

For comparative measurements of EdH and cross-product torques, an array of mechanical sensors is prefabricated through standard silicon-on-insulator processing using electron beam lithography and etching [17]. YIG disks of design thickness/diameter aspect ratio $h/d \sim 0.3$ are cut with a Ga$^+$ ion beam from a thin polished wedge, transferred by nanomanipulation onto the torque sensors, and tack welded in place with a carbonaceous ion beam-induced deposit. Monocrystalline YIG disks are a favorable choice for the demonstration: They demagnetize into a vortex state yielding
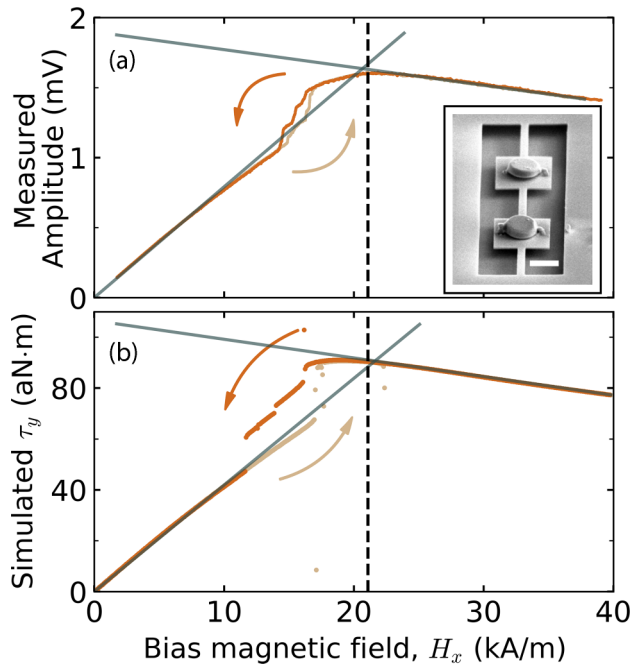
FIG. 2. Cross-product torque hysteresis loops, measured and simulated. (a) The experimental cross-product torque hysteresis of the double disk sample, driven with an rf field along $\hat{z}$ at RMS amplitude 247 ± 7 A/m. The conversion factor between lock-in signal magnitude and torque, obtained by thermomechanical calibration, is 41 ± 1 aN m/mV. A scanning electron micrograph of the sample is shown in the inset (scale bar $= 2\,\mu$m). (b) Cross-product torque hysteresis from micromagnetic simulation of a single disk of $2.0\,\mu$m diameter and $0.46\,\mu$m thickness, subject to the same rf drive amplitude used for the measurements. The torque is multiplied by two to correspond to a net magnetic volume similar to that of the sample. The two disks of the sample are far enough apart to neglect the dipole coupling between them. In (a) and (b), the solid lines show linear fits to the low-field (vortex state) and high-field (quasiuniform texture) torques. Where these lines intersect is a sensitive indicator of aspect ratio, here at approximately 21 kA/m as indicated by the vertical dashed line. The saturation moment from the measurements, as determined by comparing the peak experimental and simulated torques, is $m_\mathrm{s} = M_\mathrm{s}V = (3.0 \pm 0.1) \times 10^{-13}$ A $\cdot$ m^2.

zero cross-product torque at approximately zero DC bias field; and their low-field magnetizing curves are not complicated by pinning effects. The as-fabricated *magnetic* volumes and disk aspect ratios are somewhat lower than the physical dimensions on account of magnetically dead layers that are created by Ga beam damage to a depth of at least 50 nm under surfaces exposed to the ion flux [18]. The results reported below are from the double paddle device shown in the inset to Fig. 2, supporting two disks that are equivalent to within the fabrication uncertainty. The equations of Sec. II apply without modification to this structure. The double paddle device had the best signal transduction out of several structures that were fabricated.

The measurements are performed in vacuum at room temperature. Uniform rf magnetic fields along the y and z directions are applied using small copper wire coils wound on CNC-machined PEEK coil forms. The coil field distributions

in (A/m)/mA of coil current are calculated by finite-element rf modeling [19], and the experimental field strengths determined in separate measurements by placing a commercial in-line rf current probe (Tektronix CT-6) close to an identical coil structure outside the vacuum chamber. The phases of the rf magnetic fields at the sample are determined one drive coil at a time with the current probe. A small homemade inductive sense coil (two turns, $\sim$1.5 mm diameter) is also used to measure the relative field amplitudes from the two coils near the sample position to confirm the estimate from the finite element calculations and current amplitude measurements. The right-handedness of the field geometry is determined with the Hall probe using DC currents through the rf coils (left-handed field coordinates would introduce a minus sign for one of the torques).

Uniform DC bias fields for the precision low-field torque measurements are applied using homemade hoop electromagnets. Stronger DC fields as required for full hysteresis loops taking the YIG disks into saturation are applied using a NdFeB permanent magnet mounted on a lead screw-driven rail, with the position and orientation of the magnet computer controlled through a pair of stepper motors. DC field strengths are continuously monitored with a three-axis Hall probe during the measurements.

Mechanical displacements driven by magnetic torque are recorded through interferometric modulation of reflected optical intensity from a 633-nm beam focused near a silicon paddle edge. Torque sensitivity is calibrated via thermomechanical displacement noise at the mechanical resonance in the absence of rf torque drive. The torsional nature of the mechanical modes used for measurements are characterized by finite-element mechanical modeling [19], and confirmed through spatial maps of the signal generated by raster scanning the sample position under the laser focus. The moment of inertia of the device is asymmetric about the torsion axis, on account of the mounting of the YIG disks on top of the paddles. This asymmetry causes some hybridization of torsion and flexing motions, through angular acceleration and centripetal force. The effect on torque sensitivity is a small percentage reduction, as estimated using a three-spring toy model of the coupled modes (see Supplemental Material [20–25], Sec. S5).

A characteristic full hysteresis measurement acquired through cross-product torque is shown in Fig. 2(a) for a double paddle sensor with a disk on each paddle. The measurement is run with a phase-locked loop (PLL) to maintain the drive frequency at the same point on the mechanical resonance curve as the bias field is swept, correcting for the stiffening of the torsion mode as the Zeeman energy minimum deepens at high bias field (the drive frequency range across the measurement is 2.7882 MHz to 2.7905 MHz). The hysteresis measurement is used to constrain the magnetic aspect ratios of the disks by comparison to micromagnetic simulation [Fig. 2(b)]. Thinner disks magnetize more easily (higher positive slope at low fields [26]), and exhibit a proportionally slower decrease of torque (smaller negative slope) at high fields where the m_x moment is saturated; the rate of decrease is governed by the z-direction susceptibility, χ_z, which is larger for thicker disks. The intersection point of linear fits to the low-field and high-field torques yields a characteristic field that depends
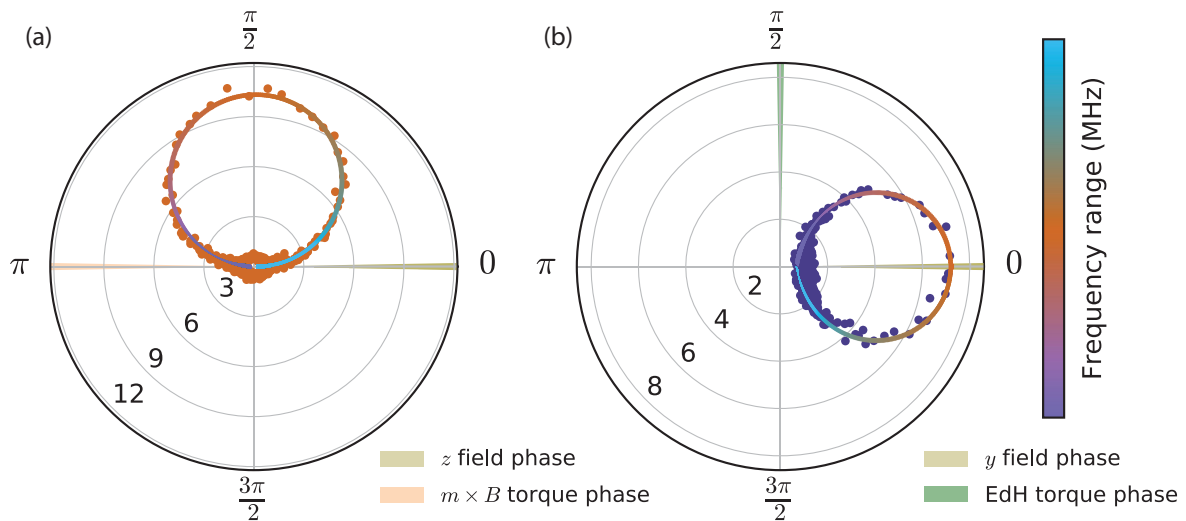
FIG. 3. Polar plots of the magnitude and phase of the signals versus frequency across the torsion resonance, for both rf drive field directions. The solid lines are fits, and through their color encode the drive frequency (color bar on the right). The drive-field phases are at zero radians in both cases. (a) The expected cross-product torque phase is π radians. The H_z^{rf}-driven signal starts in phase with the torque below resonance, and develops a phase lag of $\frac{\pi}{2}$ at resonance. (b) The expected EdH torque phase is at $\frac{\pi}{2}$, and the mechanical signal driven across resonance by H_y^{rf} behaves as in panel a) but with the overall phase rotation indicative of the EdH effect. The swept frequency range is 2.75 to 2.84 MHz (simultaneous drives with y- and z-drive frequencies separated by 3.142 kHz), and the bias magnetic field $H_x = -200$ A/m.

sensitively on the h/d aspect ratio, yielding 0.23 ± 0.01 for this sample. In the hysteretic region between 12 and 18 kA/m, where the spin texture transitions between vortex and quasi-uniform, the simulation does not represent the experiments accurately; much longer-running simulations incorporating thermal activation and the effect of magnetic edge roughness would have to be performed (see Sec. VII), and in addition the differences between the two individual disks accounted for. Away from the hysteretic region, at low and high fields where in both cases the spin texture is well-defined, the simulations are mostly very well behaved. The simulation in Fig. 2(b) includes a constant offset field $H_y = 2$ kA/m to avoid the difficulty relaxing fully to equilibrium around $H_x = 23$ kA/m seen in Fig. 7(a) when H_y is within 200 A/m of zero.

The peak measured and simulated torques are in the ratio 66 aNm/89 aNm = 0.74. This indicates that within the magnetically dead layer caused by Ga beam damage during the milling (see Supplemental Material, Sec. S1 [20]), the magnetic disks are smaller in linear dimension than the simulated disk by $\sqrt[3]{0.74} = 0.9$, or approximately 1.8 μm diameter by 0.42 μm thick.

IV. LOW BIAS FIELD VORTEX STATE EINSTEIN-DE HAAS EFFECT

Comparative frequency sweeps through the mechanical resonance, driven by H_z^{rf} (cross-product torque) and H_y^{rf} (EdH) are shown in the polar plots of Fig. 3, at a low H_x bias field where the two torques have similar magnitudes. The mechanical signal traces out an accurate resonance circle in both cases. The drive *field* phases as determined by the current probe

establish the zero radian reference of the phase angle axis and are indicated by thin wedges. The additional color markers show the corresponding cross-product and EdH drive *torque* phases predicted by Eqs. (2) and (3). Far below the resonance frequency, the torque signals begin in phase with the torque drive, as expected. The $\pi/2$ rad phase lag of the response at the peak (maximum magnitude of the resonance circle) brings the EdH-driven response back into phase alignment with the drive field on resonance, highlighting the distinct origin of this torque. There is a small constant offset on the measurement with the y-coil drive, arising from a radiative rf coupling between that coil and the photoreceiver. The resonance circle illustrates that the crosstalk phasor is constant and can be separated from the mechanical signal.

A signature measurement of the present study is shown in Fig. 4, which presents the amplitudes and phases of both radio-frequency torques as a function of bias field on either side of $H_x = 0$, demonstrating that the EdH torque easily can exceed the cross-product torque over a significant bias field range, and also the expected phase relationships for both the cross-product and EdH torques (both measured at the peak of the mechanical resonance). The linear-in-field dependence of the cross-product torque is observed, along with the bias field independence of the EdH torque. (The mechanically resonant detection in this work does not permit a direct test of the latter's linear-in-frequency dependence.) The discrete data points on the plot are determined from full frequency sweeps through the resonance at fixed bias fields, as in Fig. 3. The phases determined this way are more accurate than those from the continuous field sweeps, which exhibit run-to-run variation of the phase of about 0.1 rad. The phase-locked loop is not used here on account of the small
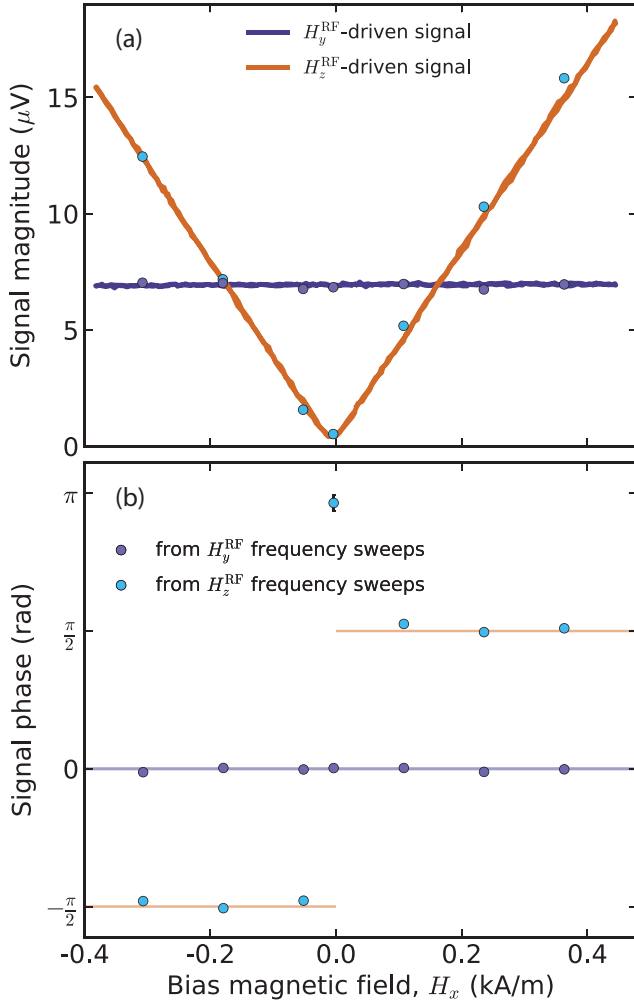
FIG. 4. Simultaneous cross-product and EdH torque measurements versus DC bias field in the low-field range from zero bias where the EdH torque dominates and through the crossover of torque magnitudes for both polarities of bias field. This illustrates (a) the measured field dependence of the torque magnitudes, as predicted from Fig. 1(b), with (b) the phase information, from the lock-in measurements. The drive frequencies are separated by 0.2 kHz for these measurements, and the 50 ms lock-in time constant ensures independent demodulation of the two signals. The discrete points are confirmation measurements from fits to frequency sweeps through the mechanical resonance acquired at fixed fields.

signals. Measurements through full 360° rotation of the in-plane field direction further highlight the qualitatively different behaviors of the two torques (see Supplemental Material, Sec. S3 [20]).

The results of Fig. 4 can be used to estimate $g\prime$ for the YIG, through comparison with the simulation results of Fig. 1. Whereas Fig. 1 assumed equal amplitude H_y^{rf} and H_z^{rf} drives, in the measurement we have $H_y^{\mathrm{rf}}/H_z^{\mathrm{rf}} = 1.41 \pm 0.05$ (see Supplemental Material, Sec. S2 [20]). For comparison of the measurements to Eq. (6), we take one-half of the bias field separation between the two points at which the EdH and cross-product torques are equal and define that as the the measured crossover field, $H_x^{\mathrm{crossover}}$ ($= 170 \pm 5$ A/m), and

therefore

$$1 = \frac{\mu_0 c_\tau \gamma\prime}{2\pi} \frac{H_x^{\mathrm{crossover}}}{f} \frac{H_z^{\mathrm{rf}}}{H_y^{\mathrm{rf}}}. \quad (7)$$

The first quotient on the right-hand side, as based on the simulations of Fig. 1 and the hysteresis measurement of Fig. 2, is determined to be [see Fig. 1(d)]

$$\frac{\mu_0 c_\tau \gamma\prime}{2\pi} = (1.3 \pm 0.1) \times 10^4 \frac{\mathrm{m}}{\mathrm{C}} \cdot g\prime. \quad (8)$$

The experimental results, jointly with the simulations to account for magnetic anisotropy, consequently arrive at the determination:

$$g\prime = \frac{f}{H_x^{\mathrm{crossover}}} \frac{H_y^{\mathrm{rf}}}{H_z^{\mathrm{rf}}} \frac{1}{(1.3 \pm 0.1) \times 10^4} \frac{\mathrm{m}}{\mathrm{C}} = 1.78 \pm 0.16. \quad (9)$$

The $g\prime$ value above is 1.5 standard deviations away from the value close to 2.0 that is to be expected based on arguments that $g - 2 \approx 2 - g\prime$, where the spectroscopic g factor for YIG is very close to the free electron value (the original determination by Dillon from ferrimagnetic resonance measurements on YIG spheres was $g = 2.005 \pm 0.002$ [27]). The dominant contributions to the uncertainty are the drive field strength ratio and the detailed magnetic shape and aspect ratio. The advantages of the microscale specimen studied here are that it demagnetizes into the vortex state and enables direct comparisons with micromagnetic simulations. It will be possible to obtain substantially improved accuracy in the determination of $g\prime$ while retaining the advantages of high mechanical frequency operation by using specimens on the order of $10\times$ larger. For these larger samples, the magnetic dead layer introduces only a very small difference between the magnetic shape and the physical shape, and by using a split coil for H_z^{rf} to reduce the dominant uncertainty in the drive field strength ratio.

A possible source of systematic error in the present experiment is an in-plane shape anisotropy that the current measurements cannot characterize; this can be addressed in future work through the incorporation of a second axis of torque detection. Note also that prior knowledge of the saturation magnetization, M_s, of YIG enters the analysis implicitly through the shape anisotropies from simulation. When all the relevant anisotropies can be characterized experimentally, $g\prime$ determinations for individual specimens through combined EdH and cross-product torque measurements will be possible without any additional inputs.

V. HIGHER BIAS FIELD VORTEX STATE EINSTEIN-DE HAAS EFFECT

Owing to the $\pi/2$ phase difference between the EdH and cross-product torques, it is possible to continue measurements of the EdH effect far beyond the crossover field, even with an rf field geometry in imperfect alignment with the mechanical coordinate system. The machining and assembly inaccuracy of ~ 10 mrad misalignment of the plane of the torsion resonators relative to the y-coil rf field direction at the sample is sufficiently small for easy separation of the unintentional admixture of cross-product torque from the raw data. At this degree of misalignment, the cross-product torque has to
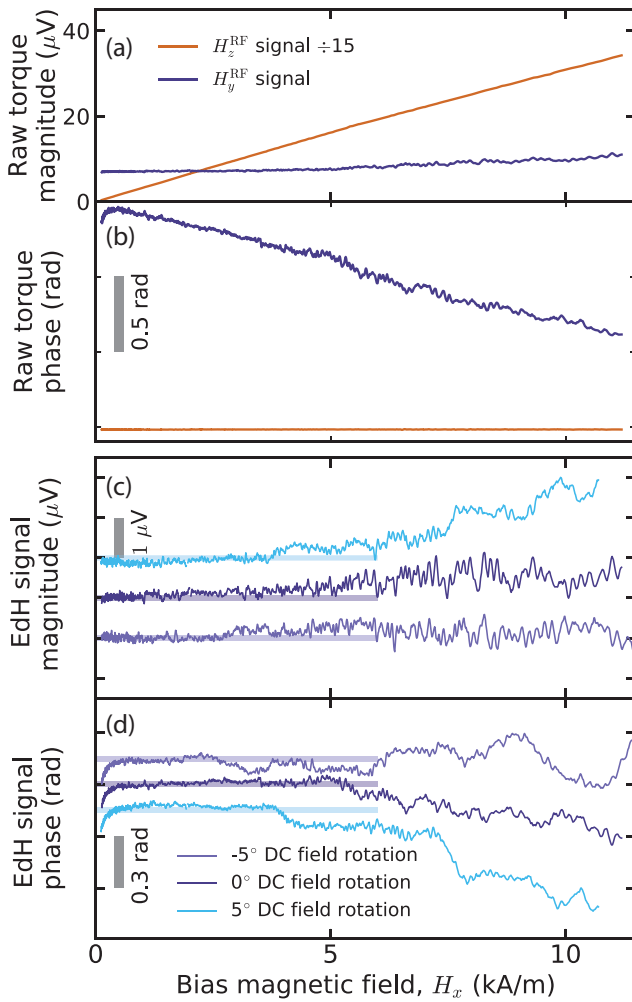
FIG. 5. Torque signals through most of the reversible, nonhysteretic bias field range where the disks remain in the vortex state for different in-plane field angles (along $\hat{x}$, and at $\pm 5°$ from $\hat{x}$). The cross-product torque (signal divided by 15) and raw H_y^{rf}-driven torque magnitudes and phases are shown in panels (a) and (b), respectively, for bias field along $\hat{x}$. The EdH torque magnitudes and phases are shown in panels (c) and (d), with the different bias field direction traces offset for clarity [offsets of $1\,\mu$V and 0.15 rad in (c) and (d), respectively]. Indications of weak vortex core pinning are revealed by the field-angle dependence arising at bias field strengths above a few kA/m. The signals are measured simultaneously, with the H_z-driven channel running in a phase-locked loop to account for the bias field-induced torsion resonance frequency shift. The small downturn of H_y-driven phase near zero bias is from the PLL beginning to have difficulty holding lock on the smallest cross-product torque signals.

develop to 100× the level of the EdH torque before the unintentional admixture makes an equal magnitude contribution to the H_y^{rf} coil-driven signal, a circumstance in which the two contributions still will separate easily and accurately in a quadrature phase-sensitive measurement.

The experimental investigation of the EdH effect to much higher DC bias fields, while remaining in the vortex spin texture, is summarized in Fig. 5. For these measurements, the PLL is running on a slightly detuned signal driven by

the H_z^{rf} coil. As the small admixture of cross-product torque driven by the H_y^{rf} coil grows linearly with increasing H_x bias field, and because this is adding in quadrature with the EdH torque, the *phase* of the resultant raw signal varies linearly [Fig. 5(b)] while its magnitude is largely unchanged [Fig. 5(a); expected to vary quadratically as the admixture slowly grows]. The EdH-only signal is isolated from the raw signal by quadrature subtraction of the H_z^{rf} coil-driven signal scaled to flatten the resulting phase at low fields. A higher-order correction, from small misalignment of the H_z^{rf} direction (versus the mechanical coordinate system) is negligible, owing to the extreme smallness of the unintentional EdH torque that the corresponding unintentional y-component drive gives rise to. The small tailing away of the extracted phase at very low bias field is an artifact from growing phase noise as the PLL approaches loss of lock.

Unexpectedly, given the absence of features suggesting magnetic disorder (Barkhausen effects) in the cross-product torque, the idealized behavior of the EdH torque persists only to bias fields of ∼3 kA/m. As seen in Figs. 5(c) and 5(d), small departures from the low-field baseline of the EdH torque emerge over the field range 3–11 kA/m. These variations depend sensitively on the in-plane bias field direction, strongly suggesting that they arise from magnetic disorder. This indicates that there is a small amount of magnetic surface roughness in the as-fabricated sample, not large enough to become visible in the cross-product torque but too large to remain invisible in the EdH torque.

Why the distinction? First, the highest energy-density regions of the vortex core are at the surfaces, creating the likelihood of interactions with surface imperfections. The core has significantly larger diameter in the center of the disk as compared to at the surfaces, owing to the thickness of the disk being approximately 25× the dipole-exchange length in this case. However, the H_z^{rf} field driving the cross-product torque is a negligible perturbation on the spin texture; it induces a very slight "breathing" of the core diameter but no modulation of the in-plane core position. If the core is encountering pinning potentials in a weakly disordered magnetic energy landscape, thermal fluctuations will drive hopping between neighboring energy minima and the rf cross-product torque will register the DC magnetic moment corresponding to the time-averaged core position. Based on the characteristic energy corrugation even in more strongly pinning systems like polycrystalline permalloy at room temperature, the hopping rate is expected to be too fast in comparison to the measurement bandwidth (determined by the lock-in time constant and filter roll-off) for telegraph noise to be visible [28].

In contrast, the H_y^{rf} drive for the EdH torque induces a direct modulation of the core position at the drive frequency. The angular frequency of the drive is five orders of magnitude higher than the largest measurement bandwidths of the present work, creating the possibility of thermally activated hopping rates to come into range of the drive frequency as the core moves across the disk (the core equilibrium position being dictated by H_x). In such circumstances, a thermally assisted, stochastic resonancelike [29,30] coherent motion of the core may result. The consequent response to the H_y^{rf} drive will exhibit enhanced amplitude and a modified phase. The emergence of these features only when the core is far enough

from the center of the disk may be indicating that the disk fabrication somehow yields greater magnetic smoothness near the centers or, alternatively, that the magnetic disorder is primarily confined to magnetic edge roughness and interaction with the disk edges becomes more important at higher bias fields as the spin texture loses its circular symmetry. The ion-milling fabrication procedure is more likely to cause an irregular disk perimeter and hence magnetic edge roughness in comparison to surface roughness. Residual small scale surface roughness will remain after polishing the YIG wedge, but what this looks like magnetically, after the development of the dead layer from ion damage, can at the present time only be speculated upon based on the measured magnetic behavior.

VI. HIGH BIAS FIELD EDH THROUGH HYSTERETIC TRANSITIONS AND IN THE QUASIUNIFORM STATE

Figure 6 shows the continuation of the EdH torque data into the quasiuniform spin texture. The unaltered magnitude and phase data from the H_y^{rf} and H_z^{rf} coils are shown [Figs. 6(a) and 6(b)] together with the resultant EdH signal after removing the cross-product admixture from the H_y coil signal [Figs. 6(c) and 6(d). At high fields, the EdH torque begins to decrease slowly, on account of the *y*-direction rf magnetic susceptibility, χ_y, slowly decreasing as the saturated moment direction becomes more strongly anchored along $\hat{x}$ in larger bias fields. As noted earlier for the case of χ_z, determining pure susceptibilities via EdH torques creates the possibility of extracting saturation moments from measured cross-product torques in high bias fields.

Surprisingly, in the hysteretic transition region between the vortex and well-saturated magnetization states, large peaks in the EdH torque (from peaks in the rf *y*-susceptibility) are observed over some ranges of H_x. The same test for signatures of magnetic disorder applies here as in the vortex state, small changes of the in-plane direction of the DC bias field. Instead of changing the trajectory of the vortex core and thereby having it explore a different cross-section of the disordered landscape, here a small rotation of where the most nonuniform regions of the spin texture are located around the disk perimeter is being effected. This gives rise to the analogous mechanism of enhancement of the susceptibility by synchronization to the rf of thermally activated hopping between pinning sites and where now the pinning broadly characterized arises from magnetic edge roughness.

The bias field rotation tests reveal a strong sensitivity to direction for the peaks beyond the last irreversible "annihilation" step in the cross-product torque at 18 kA/m, which we therefore characterize as extrinsic features. Additionally, a rotation-independent peak is seen in the returning branch of the hysteresis, just before the last irreversible "nucleation" step at 14 kA/m in the sweep from high to low field. This intrinsic feature indicates a softening of the spin texture just before nucleation, and could also be thermally assisted. Spin texture softening has been observed before in magneto-optical susceptibility measurement arrays of permalloy disks [31] and in torque-mixing susceptometry of a YIG disk [32].

The contrasting phase signatures of the putative extrinsic and intrinsic EdH torque enhancements are another impor-
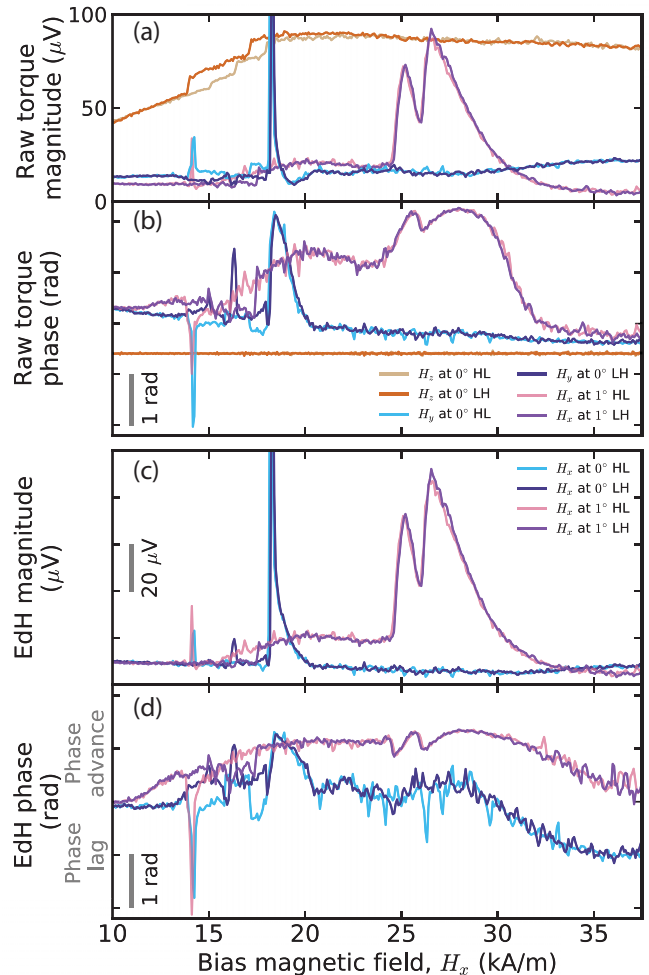
FIG. 6. The high bias field, hysteretic region of transitions in and out of the vortex state, as reflected in both EdH and cross-product torques, simultaneously measured. The direction of the bias field sweep is from low (L) to high (H) and back. The raw torque magnitudes and phases are shown in panels (a) and (b) for two in-plane bias field directions differing by only $1°$. The EdH torque magnitudes and phases, as determined by the procedure for removing the small cross-product admixture in the H_y^{rf}-driven signal, are shown in panels (c) and (d). The features in the EdH torque depending strongly on bias field strength and direction are attributed to magnetic edge roughness, thermal activation, and possibly the beginnings of domain-wall-like resonances. The clipped sections in panel (a) and (c) extend to $150\,\mu\mathrm{V}$.

tant feature. Ordinarily, one expects to find only additional phase lag (beyond that of the resonant mechanics) as a response of the system becoming unable to keep up with the pace of the rf magnetic-field drive. For example, when the drive frequency is more than negligible in comparison to the fundamental resonance of the system and the dissipation is significant, a measurable phase lag can develop simply from the physics of a damped resonator driven below resonance. Torque-mixing magnetic resonance spectroscopy (TMRS) has been performed on a sibling specimen on the same chip with a similar, single YIG disk to confirm the presence of the expected gyrotropic vortex resonance (see

Supplemental Material, Sec. S5 [20]). With the gyrotropic mode at 50 MHz and the rf drive therefore at $\sim$5% of the magnetic resonance frequency, an EdH torque phase shift of $\leqslant$0.05 rad can develop, which is consistent with the low-field observations of Figs. 4 and 5. The unpinned gyrotropic mode frequencies decrease as the DC bias field increases toward the vortex annihilation transition. In combination with high damping, this will contribute to the growing phase lag observed for some bias field directions at higher fields. The TMRS data show a fading out of the fundamental gyrotropic mode at higher fields, either an indication of stronger effective damping or, conceivably, of the onset of pinning making the gyrotropic frequencies increase [33,34]. The pinning potential in combination with thermal activation and the rf in-plane drive then gives rise to phase shifts, as already described.

The TMRS data also reveal an even lower frequency spin-resonance mode in the upper hysteresis branch (sweeping down from high field) over a narrow field range just above the vortex core nucleation transition. The signals beyond 15 kA/m in Fig. 6 make it clear, however, that the overall effect of magnetic disorder on the EdH torque phase is more complex. In particular, it is observed that the signal phase can *advance* relative to the drive phase as well as lag. This unexpected phenomenology can be motivated by noting that it is possible, in a disordered 2D energy landscape, for the arrangement of neighboring pinning sites to give rise to hops that reverse the sign of the differential (AC) magnetic susceptibility relative to the case in the absence of pinning. This has been observed for the susceptibility component parallel to the bias field [28] and can also occur for the in-plane susceptibility perpendicular to the bias field. In the case of a vortex texture, this requires a core trajectory exhibiting minor hysteresis around a local peak in the energy landscape but where the local minimum occupied after a "forward" push on one side of the peak is farther back on the other side and vice-versa—effectively changing the sign of the differential susceptibility. A related phenomenology could manifest for small closure domains.

Additional insight will come from measurements of frequency and temperature dependencies of these phenomena in future experiments. It will be highly informative to also augment the studies with an additional axis of torque detection [35]. Bearing in mind that an in-plane cross-product torque must have an anisotropy as its foundation, a sensitive angular dependence similar to that found for the EdH torque would point directly to an extrinsic source such as magnetic edge roughness. The corresponding effective torsion constants characterizing magnetic energy change versus bias field angle around such defects can have either sign, depending upon whether the extremum is a local energy maximum or minimum. Finally, it is possible that low-frequency domain-wall-like spin resonances could exist on a YIG disk periphery and couple to the mechanics, even at these comparatively small mechanical frequencies [36]. These would be accompanied by a net angular momentum absorption from the rf drive, which through suitable modulation could be detected via a torsion resonance along $\hat{x}$ (the direction of net longitudinal spin relaxation for such a mode in the present field geometry). An interesting open question is whether there is net angular momentum absorption for the case of stochastic resonance.
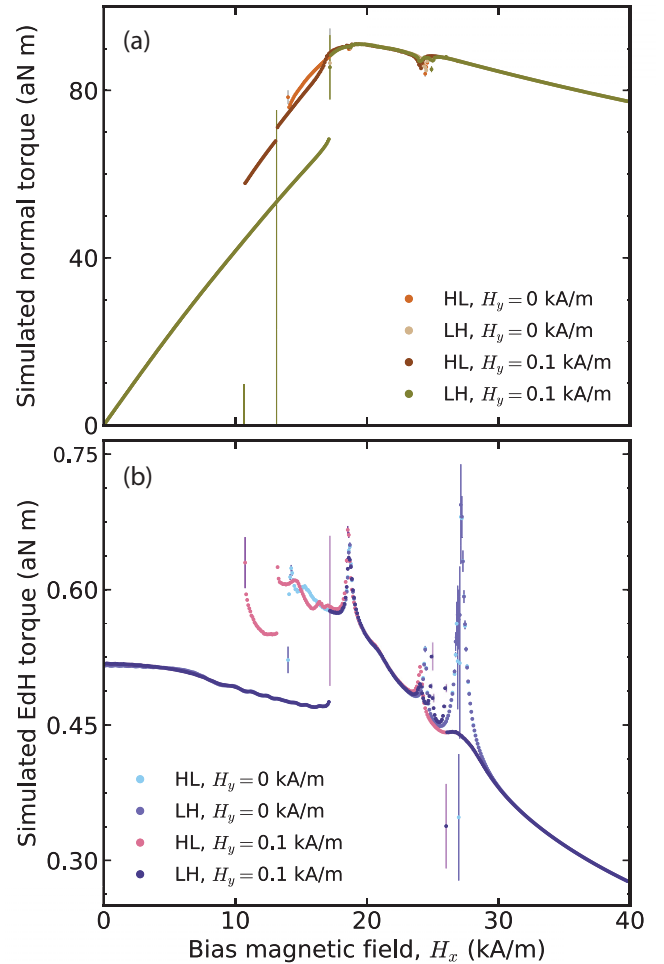
FIG. 7. Cross-product and EdH torques around the full hysteresis loop from micromagnetic simulation, using the same dimensions and drive field amplitudes as Fig. 2, for two bias field trajectories differing by a small H_y^{DC} offset (see legend). The experimental ratio $f/g' = 2.79\,\text{MHz}/1.8$ is used to calculate the EdH torque in b). HL, LH indicate the field sweep direction (high to low, low to high).

VII. SIMULATIONS

Figure 7 summarizes the current status of combined micromagnetic simulations of EdH and cross-product torques. For each bias field, H_x, in the micromagnetic simulations, small loops are computed for H_y and (separately) H_z, varying from 0 up to $+8$ A/m, down to -8 A/m, and back to 0. Efficient equilibration at each net field value is accomplished through a combination of setting a high value of the Gilbert damping constant ($\alpha = 0.5$), running a short interval (200 ps) with the Langevin temperature term [37] set to 50 K to avoid pinning in metastable states that can be caused inadvertently by the finite element grid, and finally by letting the system relax with the Landau-Lifshitz precession term disabled and $T = 0$ (MuMax3 relax() function [15]). "Raw" simulation outputs are postprocessed to extract the torques. The slope of the calculated $\vec{m} \times \mu_0\vec{H}$ versus H_z, multiplied by the experimental H_z^{rf} drive field amplitude, yields the simulated cross-product torque [Fig. 7(a)]. For the EdH effect, the simulated

rf y susceptibilities are converted to torque using Eq. (3) [Fig. 7(b)]. This approach to the simulations is predicated on the operating hypothesis that the mechanical frequency is low enough to avoid the necessity of accounting for any spin dynamics. Said hypothesis includes the assumption that spin-lattice relaxation rates, which are outside the physics described by the Landau-Lifshitz-Gilbert equation, are high enough to assume that the phase and amplitude of the resulting *mechanical* torque (the experimental measurable) is identical to that of the magnetic torque.

As mentioned in reference to Fig. 2(b), simulations of the low rf frequency range magnetic torques are most straightforward for the low- and high-field bias ranges, where the equilibrium spin texture determination is not complicated by the presence of numerous, nearly degenerate configurations. Simulated EdH torques for the vortex state reproduce the bias field-independent initial EdH torque as found in the experiments, at low fields. For the highest simulated bias fields, from 30 to 40 kA/m (well above the vortex annihilation at 18 kA/m in simulation), the spin texture is uniform enough that the simulated torques are robust against small changes in how the simulations are configured (as in the also non-hysteretic, and in other words single-valued, 0–10 kA/m range of the vortex state). It is important to bear in mind, when looking at the high field range of Fig. 7(b), that the y susceptibility remains significant after the x magnetization has saturated. A corresponding simulated EdH x-torque (parallel to the bias field) would decrease rapidly toward zero above 18 kA/m. Similarly for Fig. 7(a), the nonzero χ_z underlies the decreasing cross-product torque at high fields. χ_z is smaller than χ_y on account of the shape anisotropy, and proportionally decreases even more slowly with increasing bias field for the same reason.

The micromagnetic simulations also offer first glimpses into the more complex phenomenology of the magnetic response observed in experiment both within and neighboring the field range of hysteresis between well-defined spin textures. The step up of EdH torque after vortex annihilation in the simulations, and exhibiting hysteresis on the field-sweep down, is also seen qualitatively in the experimental behavior over the same range for the 1° field rotation data in Fig. 6(c). The dramatic peaking of experimental EdH torque over some field ranges in the quasiuniform texture is also echoed in the simulations and with Barkhausen effectlike fingerprints (sensitive to bias field magnitude and direction) that can be traced to edge roughness. The finite-element simulation employs a grid of small rectangular prisms to approximate the cylindrical disk, which incorporates into the model a simple mimic of anisotropic magnetic edge roughness sensitive to small in-plane bias field direction changes. Bias field direction changes are mimicked in the simulations presented through constant offsets of the H_y^{DC} field. Corresponding experimental measurements also have been made by setting H_x^{DC} at a fixed value and sweeping H_y^{DC} on either side of $H_y = 0$. The susceptibility peaks found in these simulations may be somewhat enhanced when the simulation encounters many nearly degenerate configurations and has more difficulty relaxing to equilibrium. The error bars in Fig. 7 are computed directly from the slope uncertainties returned by the linear fits to $\vec{m}\mu_0\vec{H}$ versus H_z and m_y versus H_y in postprocessing

of simulation output. Thus far, no simulation feature has emerged as a compelling candidate relatable to the "intrinsic" EdH torque peak found in measurements just before vortex nucleation. Future simulations must address explicitly the evolution of the torques in the time domain, as required to model phase shifts arising in slow (thermally activated) and fast (precessional) spin dynamics. Very straightforward in principle, this will require in the range of $10\times$ to $1000\times$ more GPU cycles per simulation; shortcuts such as turning off the LLG precession term apply only for the efforts to simulate equilibrium behaviors. To assist with the challenges posed by lengthier simulations, pinning effects could be added to the single domain-wall model used by Jaafar *et al.* [38] to analyze the Wallis *et al.* experiment[9]. Similarly, the analytical model of vortex core pinning [39] could be extended to include the description of EdH torques.

VIII. DISCUSSION

The results presented here underscore the combined necessity and utility of incorporating phase-sensitive detection with EdH effect measurements at radio frequencies. A great advantage, stemming from phase orthogonality of EdH and cross-product torques when the system remains in magnetic equilibrium, is the ability to separate the two in a quadrature measurement. This will prove helpful also in AC torque studies of larger (including macroscopic) magnetic specimens at lower mechanical frequencies. In practice, considerable care is required in the measurements to guard against other sources of phase shift that could cause systematic error in the EdH torque phase. Because the amplitude peak of a resonance corresponds to the point of maximum phase-versus-frequency slope, the effects of mechanical frequency shifts as caused by the Zeeman energy of the sample changing with DC bias field, and from temperature drift of the sensor, must be removed. One means of stabilizing the measurements against phase shifts other than those arising directly in the EdH torque, as demonstrated here, is tracking a cross-product torque simultaneously in the same mechanical mode, using a phase-locked loop.

Scaling a given sensor geometry to smaller linear dimensions, both increase the resonance frequencies and improve the absolute torque sensitivity. Since the absolute sensitivities of small torque sensors are sufficient to overcome the cubic decrease of sample volume with linear downscaling [40], small devices are particularly effective at discriminating EdH from other effects. Applied field uniformity is easier to achieve over small sample volumes as well, improving the isolation from unintentional torques and gradient forces.

The twisting motion of the sensor induces a back-action on the magnetization through the Barnett effect. The magnitude of this back-action is negligible here (and indeed would be invisible to the measurements where the simultaneous torque drives have a slight frequency detuning relative to one another) but it is useful to develop a feel for the numbers for future reference. The scale of the shift in ground-state energy from rotation is $\mu_0 m H_\Omega$, where angular velocity Ω gives rise to the effective field (or, in Barnett's words, "intrinsic

magnetic intensity of rotation") [11,41,42]:

$$H_\Omega = \frac{2m_e}{\mu_0 e g'}\Omega = \frac{4\pi m_e}{\mu_0 e}\frac{f^{rot}}{g'}. \qquad (10)$$

The numerical prefactor is the inverse of the scale-setting factor from Fig. 1(d), here $1/17588 = 5.686 \times 10^{-5}$ C/m. For harmonic angular motion of the torque sensor this is a sinusoidal effective field with f^{rot} representing the instantaneous rotational velocity in cycles per second. In the present experiments, the angular displacement amplitudes remain less than 1 mrad even when driven by the maximum cross-product torques (see Supplemental Material, Sec. S5 [20]). For the resonant frequency of 2.8 MHz, this corresponds to peak rotational speeds $f^{rot} \sim 2.8 \times 10^3$ s^{-1}, yielding a characteristic $H_\Omega \sim 0.08$ A/m. The scale of H_Ω is 10^{-3} times smaller than the rf field driving the mechanical motion. This is not significant here, but must be borne in mind for experiments where, as an example, higher mechanical Q yields larger displacement per unit driving field.

It will be highly desirable in some future experiments to have a *second*, orthogonal torque detection axis. As already noted, these include the characterization of additional anisotropies and the determination of when there is a net angular momentum absorption from the driving rf field. Elaborating upon the latter, detection of spin resonances (which may be viewed as frequency-specific anisotropies) via the EdH effect is a powerful and underutilized technique. The results presented here demonstrate the possibility of direct detection of spin resonances through EdH torques along the axis of the rf magnetic field, through the magnetic susceptibility enhancement on resonance (and assuming that the sensor has sufficient torque sensitivity at that frequency). In addition, in a conventional magnetic resonance, there is a steady flow of angular momentum into the spin system from rf absorption under continuous driving, effectively corresponding to a DC EdH torque parallel to the bias magnetic field and *perpendicular* to the rf. Modulation of this DC torque at some low mechanical frequency underpins the successful torque detection of resonance pioneered by Alzetta *et al.* and Ascoli *et al.* [43,44]. Torque-mixing magnetic resonance spectroscopy [45], on the other hand, is effectively an rf-modulated implementation of the direct rf-EdH measurements reported here. The development of TMRS preceded the exploration of EdH manifestations at lower rf frequencies reported here, spanning frequencies from well-below to those approaching the lowest magnetic resonance mode. Here, the mechanical (and hence rf drive) frequency remains constant while the frequency of the lowest magnetic resonance is tuned via the DC bias field (and in a manner dependent upon the spin texture). Implementing the measurements with a second torque axis will enable direct intercomparisons between the different detection modalities, with the possibility of shedding new light on spin dynamics including spin-lattice relaxation mechanisms and their anisotropies. It will also become possible to measure g and g' in a single mechanically based experiment on the same sample, enabling important questions from the earliest days of spin dynamics [6,46] to be revisited for materials of contemporary interest.

IX. SUMMARY

The EdH experiment was a milestone in magnetism, demonstrating the intrinsic connection between net magnetization and mechanical angular momentum. The expected angular momentum change upon reversing magnetization, within the Amperian molecular current model for magnetic moment, was small and drove Einstein and de Haas to undertake a mechanically resonant AC measurement wherein the angular displacement of a torsion balance would grow upon synchronous alternation of the poling direction of a supported magnet. With the torque felt by the sensor proportional to the time rate of change of angular momentum, the challenge of discriminating the EdH torque from small, net cross-product torques arising through imperfect symmetry and/or parallelism of the magnetic field and sample geometries is exacerbated at low mechanical frequencies. This possibly accounts for the original publication reporting a torque magnitude approximately $2\times$ larger than the true value determined by later experiments. The measurements reported here establish the torque phase as an equally important observable. Phase can be used to differentiate between sources of AC torque. To summarize one of the main findings of the present work: If Einstein and de Haas, hypothetically, had been able to measure signal phases, it is very likely that they would not have observed the phase expected from the molecular current model for the origin of magnetism, and therefore would not have been able to report the model's confirmation.

Additionally, at the much higher frequencies of nanomechanical resonances, the EdH torques are much larger in proportion and it becomes easier, in a relative sense, to engineer the DC and rf applied field geometries required for adequate suppression of artifacts from other sources of mechanical drive. All else being equal, the ratio of EdH to other magnetic torques increases linearly with the mechanical frequency. The linear scaling with frequency of EdH torque magnitudes cannot continue without limit, however, and it is precisely through the breakdown of such scaling that the methods will become most powerful and interesting. Here again, careful attention to the signal phase will be of utmost importance: The onset of a phase lag at high enough drive frequencies could be the first indication of an intrinsic, limiting, relaxation rate, before the sublinear evolution of signal magnitude is detected versus drive frequency. Direct mechanically based studies of spin-lattice dynamics in certain ordered magnetic systems may be on the not-too-distant horizon. A recent theoretical study of the role of phonon spin in the EdH effect has discussed conditions for decoupling of that contribution [47].

Together, these features could elevate EdH measurements to the level of a mainstream tool in nanomagnetism, directly applicable to sensitive measurements of magnetic susceptibility in anisotropic systems, and ultimately even for the determination of spin-lattice relaxation times in magnetically ordered (nonparamagnetic) states. The radio-frequency behaviors of EdH torque represent another example, beyond miniaturization of earlier work, of the opportunities created by nanoscience to expose and explore new physics. Pure spin-mechanical, torque-mediated measurements in a magnetism laboratory-on-a-chip implementation as envisioned by

Moreland [48] are poised to mine magnetic information in surprising depth.

ACKNOWLEDGMENTS

[1] A. Einstein and W. J. de Haas, Experimental proof of the existence of Ampere's molecular currents, Proceedings of the Royal Netherlands Academy of Arts and Sciences (KNAW), 18, 696 (1915).

[2] J. Q. Stewart, The moment of momentum accompanying magnetic moment in iron and nickel, Phys. Rev. **11**, 100 (1918).

[3] S. J. Barnett, Gyromagnetic and electron-inertia effects, Rev. Mod. Phys. **7**, 129 (1935).

[4] G. G. Scott, Review of gyromagnetic ratio experiments, Rev. Mod. Phys. **34**, 102 (1962).

[5] P. Galison, *How Experiments End* (University of Chicago Press, Chicago, IL, 1987).

[6] C. Kittel, On the gyromagnetic ratio and spectroscopic splitting factor of ferromagnetic substances, Phys. Rev. **76**, 743 (1949).

[7] B. D. Cullity and C. D. Graham, *Introduction to Magnetic Materials*, 2nd ed., edited by L. Hanzo (John Wiley & Sons, Hoboken, NJ, 2008).

[8] R. N. Kleiman, G. K. Kaminsky, J. D. Reppy, R. Pindak, and D. J. Bishop, Single-crystal silicon high-q torsional oscillators, Rev. Sci. Instrum. **56**, 2088 (1985).

[9] T. M. Wallis, J. Moreland, and P. Kabos, Einstein-de Haas effect in a NiFe film deposited on a microcantilever, Appl. Phys. Lett. **89**, 122502 (2006).

[10] K. Harii, Y.-J. Seo, Y. Tsutsumi, H. Chudo, K. Oyanagi, M. Matsuo, Y. Shiomi, T. Ono, S. Maekawa, and E. Saitoh, Spin Seebeck mechanical force, Nat. Commun. **10**, 2616 (2019).

[11] M. Arabgol and T. Sleator, Observation of the Nuclear Barnett Effect, Phys. Rev. Lett. **122**, 177202 (2019).

[12] H. Chudo, K. Harii, M. Matsuo, J. Ieda, M. Ono, S. Maekawa, and E. Saitoh, Rotational doppler effect and Barnett field splitting in spinning NMR, J. Phys. Soc. Jpn. **84**, 043601 (2015).

[13] R. I. Joseph, Ballistic demagnetizing factor in uniformly magnetized cylinders, J. Appl. Phys. **37**, 4639 (1966).

[14] M. Beleggia, M. De Graef, and Y. T. Millev, Demagnetization factors of the general ellipsoid: An alternative to the Maxwell approach, Philos. Mag. **86**, 2451 (2006).

[15] A. Vansteenkiste, J. Leliaert, M. Dvornik, M. Helsen, F. Garcia-Sanchez, and B. Van Waeyenberge, The design and verification of MuMax3, AIP Adv. **4**, 107133 (2014).

[16] B. Christensen and J. C. Price, NMR line shape of 29Si in single-crystal silicon, Phys. Rev. B **95**, 134417 (2017).

[17] Z. Diao, J. E. Losby, J. A. J. Burgess, V. T. K. Sauer, W. K. Hiebert, and M. R. Freeman, Stiction-free fabrication of lithographic nanostructures on resist-supported nanomechanical resonators, J. Vac. Sci. Technol. B **31**, 051805 (2013).

[18] A. E. Fraser, Focused Ion Beam Milled Magnetic Cantilevers, master's thesis, University of Alberta, 2010.

[19] COMSOL Multiphysics® v. 5.4 (COMSOL AB, Stockholm, Sweden).

[20] See Supplemental Material at http://link.aps.org/supplemental/10.1103/PhysRevB.102.054415 for descriptions of device fabrication, rf coil geometries, additional experimental data, and torque sensitivity calibration, which includes Refs. [21–25].

[21] Shin-Etsu YIG lot no. sew-3571 (Shin-Etsu Chemical Co., Ltd., Tokyo, Japan).

[22] J. E. Losby, J. A. J. Burgess, Z. Diao, D. C. Fortin, W. K. Hiebert, and M. R. Freeman, Thermo-mechanical sensitivity calibration of nanotorsional magnetometers, J. Appl. Phys. **111**, 07D305 (2012).

[23] B. D. Hauer, C. Doolin, K. S. D. Beach, and J. P. Davis, A general procedure for thermomechanical calibration of nano/micro-mechanical resonators, Ann. Phys. **339**, 181 (2013).

[24] M. R. Freeman, Method for measuring current distribution in an integrated circuit by detecting magneto-optic polarization rotation in an adjacent magneto-optic film, U.S. Patent No. 5,663,652 (1997).

[25] S. R. Compton, Nanofabrication methods towards a photonically-based torque magnetometer for measurement of individual single-crystalline yttrium iron garnet structures, master's thesis, University of Alberta, 2012.

[26] R. P. Cowburn, D. K. Koltsov, A. O. Adeyeye, M. E. Welland, and D. M. Tricker, Single-Domain Circular Nanomagnets, Phys. Rev. Lett. **83**, 1042 (1999).

[27] J. F. Dillon, Ferrimagnetic resonance in yttrium iron garnet, Phys. Rev. **105**, 759 (1957).

[28] J. A. J. Burgess, A. E. Fraser, F. Fani Sani, D. Vick, B. D. Hauer, J. P. Davis, and M. R. Freeman, Quantitative magneto-mechanical detection and control of the Barkhausen effect, Science **339**, 1051 (2013).

[29] M. I. Dykman, R. Mannella, P. V. E. McClintock, and N. G. Stocks, Phase Shifts in Stochastic Resonance, Phys. Rev. Lett. **68**, 2985 (1992).

[30] L. Gammaitoni, M. Martinelli, L. Pardi, and S. Santucci, Observation of Stochastic Resonance in Bistable Electron-Paramagnetic-Resonance Systems, Phys. Rev. Lett. **67**, 1799 (1991).

[31] J. A. J. Burgess, D. C. Fortin, J. E. Losby, D. Grombacher, J. P. Davis, and M. R. Freeman, Thermally activated decay of magnetic vortices, Phys. Rev. B **82**, 144403 (2010).

[32] J. E. Losby, Z. Diao, F. Fani Sani, D. T. Grandmont, M. Belov, J. A. J. Burgess, W. K. Hiebert, and M. R. Freeman, Nanomechanical AC susceptometry of an individual mesoscopic ferrimagnet, Solid State Commun. **198**, 3 (2014).

[33] R. L. Compton and P. A. Crowell, Dynamics of a Pinned Magnetic Vortex, Phys. Rev. Lett. **97**, 137202 (2006).

[34] T. Y. Chen, M. J. Erickson, P. A. Crowell, and C. Leighton, Surface Roughness Dominated Pinning Mechanism of Magnetic Vortices in Soft Ferromagnetic Films, Phys. Rev. Lett. **109**, 097202 (2012).

[35] G. Hajisalem, J. E. Losby, G. de Oliveira Luiz, V. T. K. Sauer, P. E. Barclay, and M. R. Freeman, Two-axis cavity optomechanical torque characterization of magnetic microstructures, New J. Phys. **21**, 095005 (2019).

[36] E. Saitoh, H. Miyajima, T. Yamaoka, and G. Tatara, Current-induced resonance and mass determination of a single magnetic domain wall, Nature (London) **432**, 203 (2004).

[37] J. Leliaert, J. Mulkers, J. De Clercq, A. Coene, M. Dvornik, and B. Van Waeyenberge, Adaptively time stepping the stochastic Landau-Lifshitz-Gilbert equation and nonzero temperature: Implementation and validation in MuMax3, AIP Adv. **7**, 125010 (2017).

[38] R. Jaafar, E. M. Chudnovsky, and D. A. Garanin, Dynamics of the Einstein-de Haas effect: Application to a magnetic cantilever, Phys. Rev. B **79**, 104410 (2009).

[39] J. A. J. Burgess, J. E. Losby, and M. R. Freeman, An analytical model for vortex core pinning in a micromagnetic disk, J. Magn. Magn. Mater. **361**, 140 (2014).

[40] J. E. Losby, V. T. K. Sauer, and M. R. Freeman, Recent advances in mechanical torque studies of small-scale magnetism, J. Phys. D: Appl. Phys. **51**, 483001 (2018).

[41] S. J. Barnett, Magnetization by rotation, Phys. Rev. **6**, 239 (1915).

[42] Y. Ogata, H. Chudo, M. Ono, K. Harii, M. Matsuo, S. Maekawa, and E. Saitoh, Gyroscopic g factor of rare earth metals, Appl. Phys. Lett. **110**, 072409 (2017).

[43] G. Alzetta, E. Arimondo, C. Ascoli, and A. Gozzini, Paramagnetic resonance experiments at low fields with angular-momentum detection, Il Nuovo Cimento **52**, 392 (1967).

[44] C. Ascoli, P. Baschieri, C. Frediani, L. Lenci, M. Martinelli, G. Alzetta, R. M. Celli, and L. Pardi, Micromechanical detection of magnetic resonance by angular momentum absorption, Appl. Phys. Lett. **69**, 3920 (1996).

[45] J. E. Losby, F. Fani Sani, D. T. Grandmont, Z. Diao, M. Belov, J. A. J. Burgess, S. R. Compton, W. K. Hiebert, D. Vick, K. Mohammad, E. Salimi, G. E. Bridges, D. J. Thomson, and M. R. Freeman, Torque-mixing magnetic resonance spectroscopy, Science **350**, 798 (2015).

[46] J. Van Vleck, The coupling of angular momentum vectors in molecules, Rev. Mod. Phys. **23**, 213 (1951).

[47] A. Ruckriegel, S. Streib, G. E. W. Bauer, and R. A. Duine, Angular momentum conservation and phonon spin in magnetic insulators, Phys. Rev. B **101**, 104402 (2020).

[48] J. Moreland, New prospects for quantitative magnetometry at the nanoscale, invited talk at Magnetic North III, Banff, AB, Canada, 2012.